Ceramics International 50 (2024) 43788–43799

Contents lists available at ScienceDirect

Ceramics International

journal homepage: www.elsevier.com/locate/ceramint

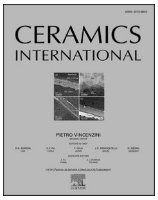

Ruthenium-doped ZnO nanostructures: Growth, characterization, and applications in waveguides and light-emitting devices

Rodríguez-Peña Micaela [*], Sotillo Belén, Urbieta Ana, Fernández Paloma

Depto. de Física de Materiales, Facultad de Físicas, Univ. Complutense, 28040 Madrid, Spain

ARTICLE INFO

Handling editor: Dr P. Vincenzini

Keywords:
ZnO (D)
Defects (B)
Optical properties (C)
Electron microscopy (B)

ABSTRACT

ZnO based materials are gaining importance due to its potential applications. In many of these applications, the size, shape and dopability of the structures grown play a determinant role. In the present work, ZnO nano- and microstructures doped with Ru have been grown using the Vapour-Solid (VS) method. Among the different growth parameters, gas flux and initial dopant content seem to play the major role to determine both shape and size of the structures. The main morphologies obtained are self-arranged triangular grids and elongated structures. Based on microscopic observations a simplified growth model is proposed for the grids. An exhaustive characterization has been performed. X-Ray diffraction (XRD) investigations demonstrate good crystallinity and texturing related to preferential growth direction changes due to doping. Luminescence characterization through photo- and cathodoluminescence (PL and CL) techniques reveals typical ZnO near band edge and deep level emission bands at 3.2 and 2.3 eV, respectively. The potential use of elongated structures as waveguides and optical cavities, Fabry-Pèrot resonators, is explored.

1. Introduction

In the last few decades, attention has been drawn to wide gap semiconductors due to the necessity to create ultraviolet (UV) and blue optical devices. ZnO, a II-VI semiconductor, is a very suitable candidate since it has a wide bandgap (3.37 eV) and an exciton energy of 60 mV, favoring efficient excitonic emission processes at room temperature [1]. Good examples of these applications are the work of F. Rahman [2], which reviews how this material has been used for the manufacture of LED emitters. M. H. Huang et al. reported room-temperature UV laser emission from a ZnO nanowires array [3]. On the other hand, due to its high refractive index, zinc oxide is an excellent candidate for creating resonant microcavities and light guides [4]. Among the wide variety of morphologies, those with a hexagonal shape have attracted special attention as resonant cavities [5,6].

In recent years, doped zinc oxide structures have been extensively studied due to their advantageous properties and the variety of morphologies that can be achieved through doping. The incorporation of dopant ions to different crystalline planes leads to changes in the surface energy, modifying the preferential growth directions of the wurtzite structure and, thus, promoting the appearance of new morphologies that are not usually observed in non-doped ZnO. In this way, needles, ribbons, flowers, rods or boxes have been obtained using different growth methods and dopants [7]. Since the optical resonant behavior of the structures depends on their shape, the possibility of controlling the final form of the cavities changing the type of dopant used opens up their applicability to fabricate new optical devices. In fact, optical resonators in rare earth (Er, Tb and Eu) or alkaline (Li, K) doped ZnO with different morphologies have been investigated in previous works [6,8–11].

Among transition metals, ruthenium, belonging to the platinum group, has stood out in its efficiency for several applications [12]. Within the wide range of possibilities offered by ruthenium doped zinc oxide, it is possible to find this material acting as photocatalyst [13–16], electrocatalyst [17], hydrogen and methanol production [18] and forming Ru-doped ZnO/p-Si heterojunctions [19]. The incorporation of Ru to ZnO can also increase its electrical conductivity due to the excess of charge of the substitutional dopant ions and the different oxidized states that Ru can adopt. This fact plays an important role in the fabrication of spintronic devices with new magnetic materials based on Transition Metal Oxides (TMOs) [20,21]. Optical properties of Ru doped ZnO have been already analyzed [22,23], and some theoretical studies have tried to shed light on the electronic structure of ZnO:Ru by first principles calculation and density functional theory (DFT) [24,25] but a lot of research work is needed to elucidate the influence of the

---

[*] Corresponding author. Depto. de Física de Materiales, Facultad de Físicas, Plaza de Ciencias, 1, Ciudad Universitaria, 28040 Madrid, Spain.
E-mail address: micaelar@ucm.es (R.-P. Micaela).

https://doi.org/10.1016/j.ceramint.2024.08.232
Received 27 April 2024; Received in revised form 27 July 2024; Accepted 13 August 2024

Table 1
Notation and growth conditions of the samples.

	Initial RuO_2 content (wt.%)	Initial atomic percentage of Ru (at.%)	Nitrogen flow (l/min)
1L	1	0.31	0.5
5L	5	1.6	0.5
10L	10	3.24	0.5
1H	1	0.31	1.5
5H	5	1.6	1.5
10H	10	3.24	1.5

incorporation of ruthenium into the ZnO lattice.

In this paper, we will carry out a study of the luminescent properties of the material, providing a deeper knowledge of the material and unravelling the implication of ruthenium. The samples have been grown by a Vapour-Solid method (VS). This mechanism is widely employed for the growth of one-dimensional or quasi-one-dimensional structures and is based on the evaporation and subsequent deposit of the material either on cooler regions or on preferential nucleation sites onto the substrate. Since no catalyst is used, the grown structures have a high crystalline quality and are free from contaminants as occur in other

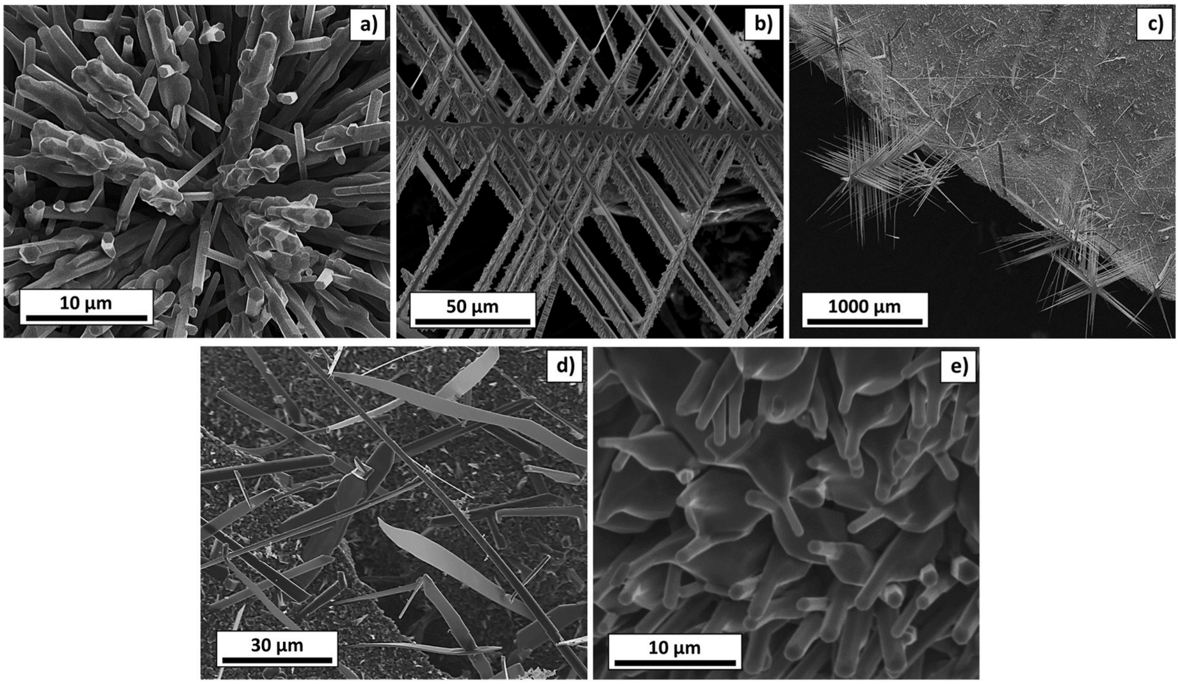

Fig. 1. SE images of the characteristic morphologies of (a, b) 1 wt %, (c) 5 wt % and (d, e) 10 wt % Ru doped ZnO samples of low flux treatments (0.5 l/min).

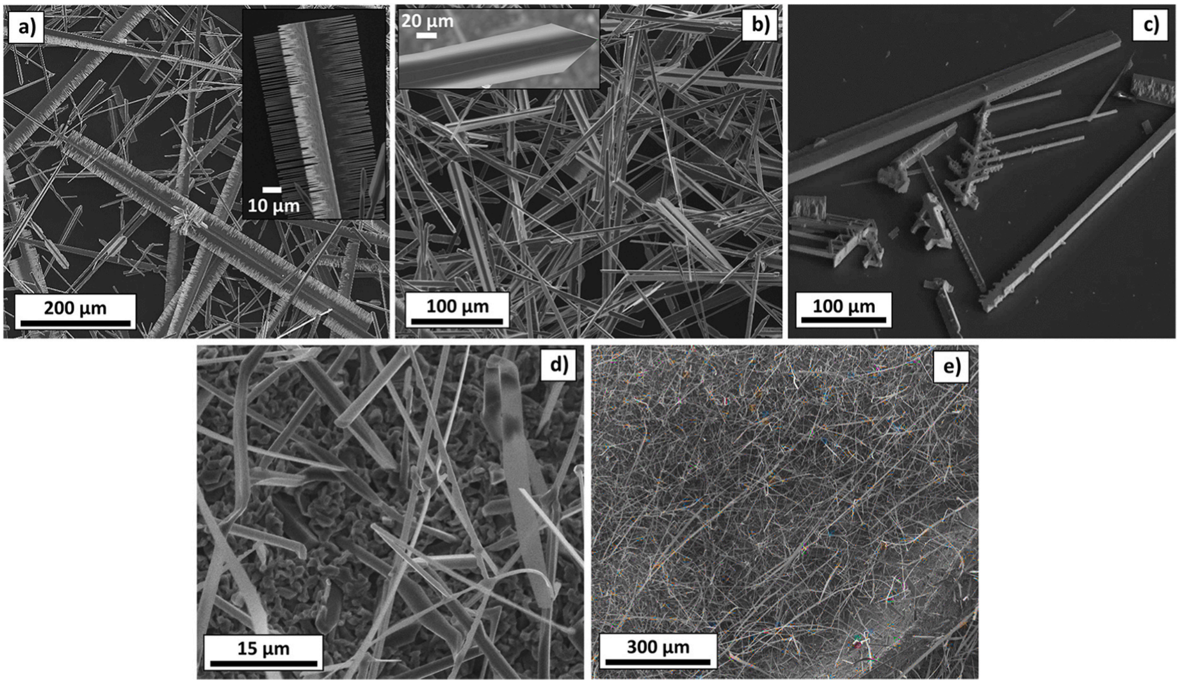

Fig. 2. SE images of the characteristic morphologies of (a, b) 1 wt %, (c) 5 wt % and (d, e) 10 wt % Ru doped ZnO samples of high flux treatments (1.5 l/min).

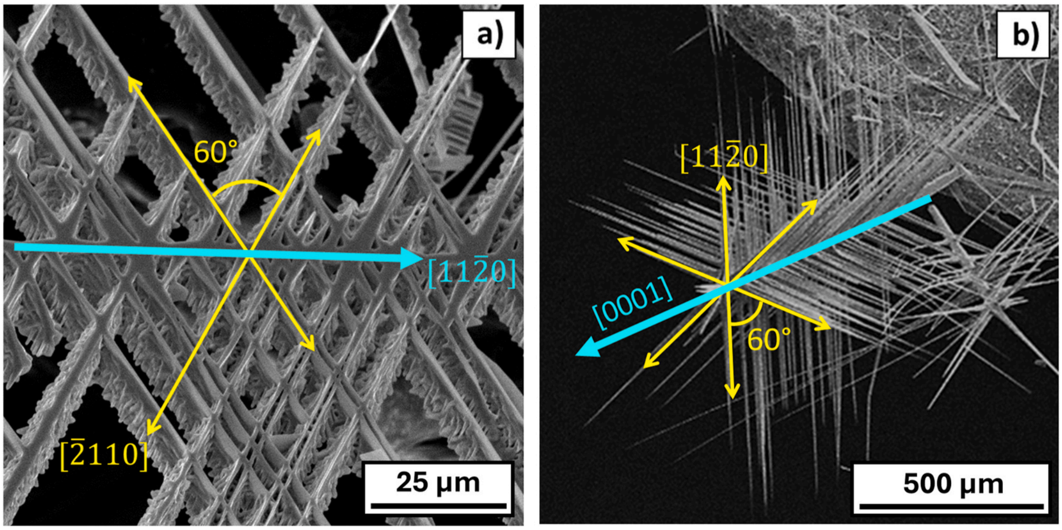

Fig. 3. Illustration of the crystal arrangement of two typical morphologies belonging to (a) 1L and (b) 5L samples.

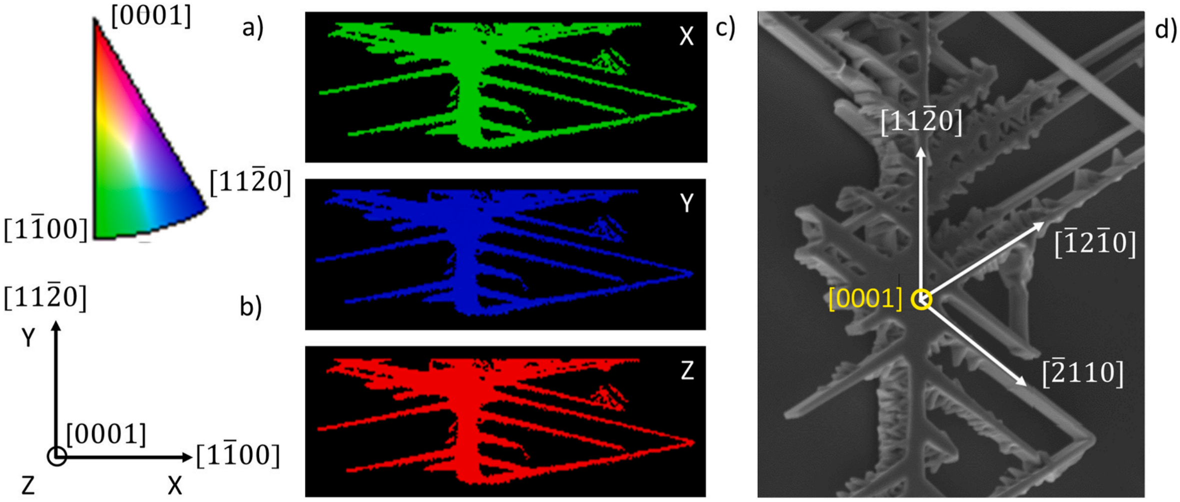

Fig. 4. a) Legend of scale color applied to EBSD maps. b) Detector axes with the associated crystalline directions of the grid. c) EBSD color maps. Each image represents the orientation of the sample along the axis indicated in the top right corner. d) SE image showing the growth directions of each part of the structure. (For interpretation of the references to color in this figure legend, the reader is referred to the Web version of this article.)

synthesis methods such as Vapour-liquid-solid (VLS) [26]. In addition, we show how to leverage the high refractive index of the material to build waveguides and optical cavities, giving a perspective of possible applications for elongated Ru doped ZnO structures. This is one of the mains strengths of the paper since very few studies on the optical behavior of ZnO:Ru has been done up to date.

2. Experimental method

2.1. Synthesis of ruthenium doped ZnO structures

Precursor powders were composed of a mixture of zinc sulphide, ZnS, (Sigma-Aldrich, 99.99 %) and ruthenium oxide, RuO_2, (Sigma-Aldrich, 99.9 %) in variable proportions. To study the effect of doping incorporation, three weight percentages of ruthenium oxide were selected: 1 % wt, 5 % wt and 10 % wt. To ensure the equivalence of the different samples used as source/substrate, 2 g of mixture is prepared, then equivalent amounts are taken to press several pellets. Powders were homogenized through mechanical milling during 5 h at 180 rpm in a centrifugal ball mill (Retsch S100, Haan, Germany) with 20 mm agate balls, and then compacted forming disk-shaped pellets (diameter: 7 mm, thickness:3 mm) using a hydraulic press (Mega KP-30A). After that, the samples were individually annealed on an alumina boat inside a horizontal tubular furnace (C.H.E.S.A. Microtest, Spain) at 950 °C for 10 h under a constant N_2 flow. Temperature and gas flow are the parameters that determine the predominant morphology of the structures. In this case, temperature has been set to 950 °C as it is the best compromise temperature-time to obtain large densities of structures. Two sets of samples have been grown under different fluxes (0.5 l/min and 1.5 l/min, named low (L) and high (H) flux, respectively) to obtain the different morphologies reported in this work. The notation of the samples and growth conditions are shown in Table 1. As a result of this thermal treatment, micro- and nanostructures were grown forming a crust over the compacted powders, as well as partially covering the alumina boat.

2.2. Characterization techniques

Morphology was analyzed by means of secondary electron images, recorded in FEI Inspect Microscope. The composition of the samples was

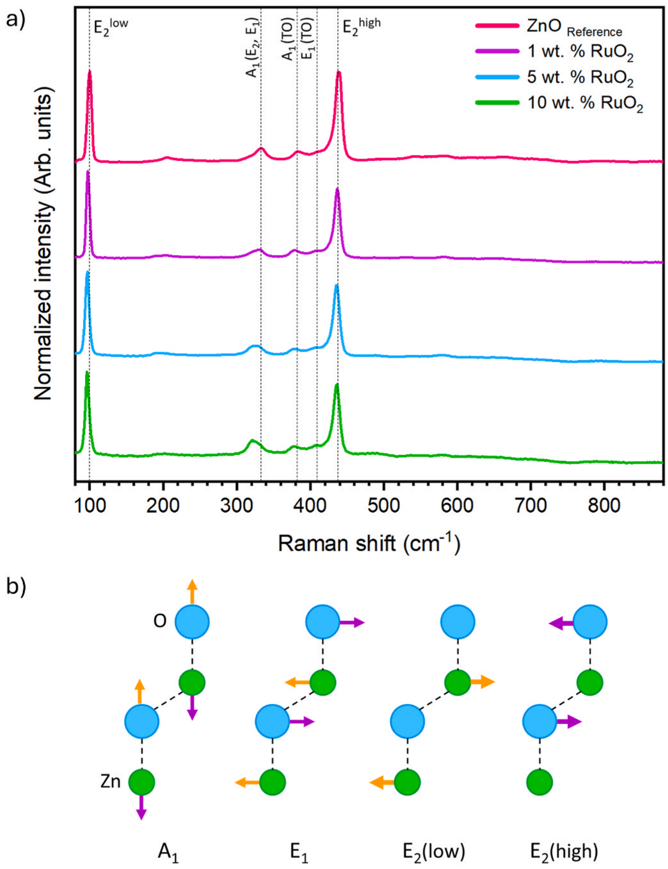

Fig. 5. a) μ- Raman spectra of the structures obtained from Ru doped ZnO. Pure ZnO spectrum is also shown for comparison. b) Schematic representation of identified modes of vibration of ZnO on μ- Raman spectra.

studied by X-Ray Microanalysis (EDX) in a LEICA Stereoscan 440 with a Bruker AXS Quantax system attached. X-ray Diffraction was carried out in a PANalytical Empyrean diffractometer using Cu-Kα radiation. μ-Raman spectroscopy experiments were performed in a confocal optical microscope Horiba Jobin Yvon LabRAM HR800 operating with a red He–Ne laser at $\lambda = 632.8$ nm. Cathodoluminescence spectra and images were recorded on a HITACHI S2500 and on the LEICA Stereoscan 440, respectively. Spectra have been recorded with a CCD camera HAMAMATSU PMA-11, while images have been registered with a HAMAMATSU R-928 photomultiplier and MATELECT amplifier. μ-Photoluminescence (μ-PL) was carried out at the confocal optical microscope Horiba Jobin Yvon LabRAM HR800 but using a He–Cd ultraviolet laser at $\lambda = 325$ nm as excitation source. All measurements were performed at room temperature.

3. Results and disscussion

In this work we have studied the effect of two main factors on the morphology of the structures: the gas transport flux and the dopant concentration.

As a general observation, the gas transport flux seems to play the major role on determining the morphology of the structures. In all cases, the predominant structures present elongated shapes. The morphologies obtained in the different flux conditions (L: Fig. 1; H: Fig. 2) might be grouped into 6 main morphologies: hexagonal columns, rods, ribbons, needles, wires and elongated structures with secondary growths. Ribbons and wires have large aspect ratios. Ribbons have average dimensions of 300 μm in length, while their widths present a large dispersion (500 nm - 5 μm). Wires have a similar lengths and diameters around 1 μm. Regarding the dopant concentration, a strong dependence of the morphology is also observed, although with less variability. At low dopant concentrations, the structures keep the hexagonal habit characteristic of the host material, ZnO with a wurtzite structure. As the ruthenium content increases, the hexagonal habit is progressively lost and the secondary growth is more frequent.

Let's now analyze the different morphologies in a closer detail. Typical structures obtained for different Ru content under low flux conditions are shown in Fig. 1. In sample 1L, we found hexagonal rods with rod-like secondary growths with diameters below 3 μm and lengths from 10 to 30 μm (Fig. 1 a). More interestingly, grids formed by interconnected ribbons are present (Fig. 1 b), similar to those observed by Y. Ortega et al. using aluminum as dopant for zinc oxide [27]. In our case, dimensions of grids may reach several hundreds of micrometers, but the boxes which compose the grids are only few tens of microns in size. In sample 5L, sixfold star-like structures, whose arms can be as long as 700 μm, are observed (Fig. 1 c). At the maximum ruthenium content, sample 10L, the order is partially lost due to the strain induced by the dopant. The ionic radius of ruthenium (coordination VI) is 0.68 Å while that of

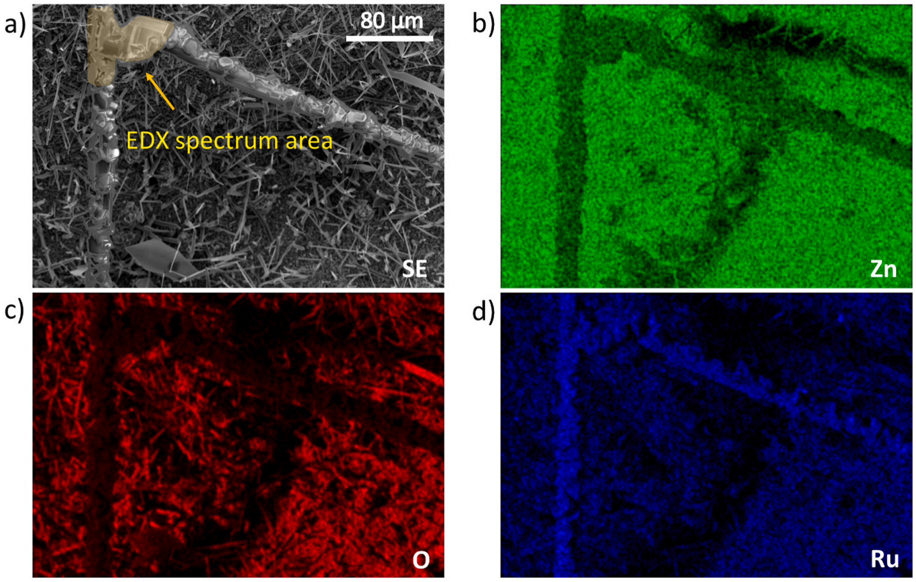

Fig. 6. SE image (a) and EDX mappings of Zn (b), O (c) and Ru (d) of a structure grown on a sample with 10 % wt. of RuO_2.

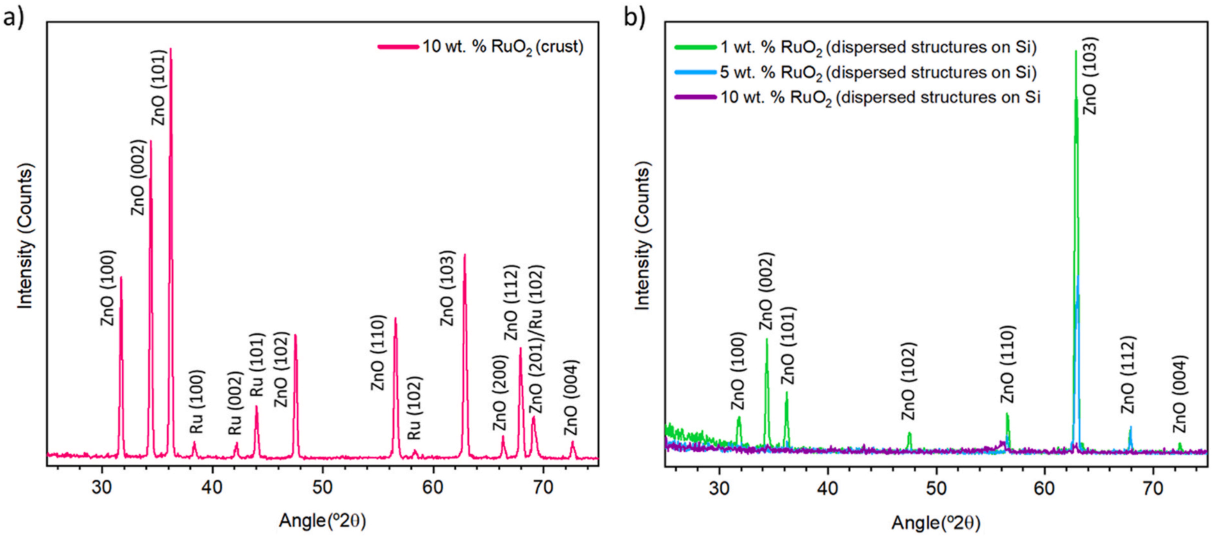

Fig. 7. XRD pattern of a) crust of the sample prepared with 10 wt % RuO2 and b) structures on Si from Ru-doped ZnO samples.

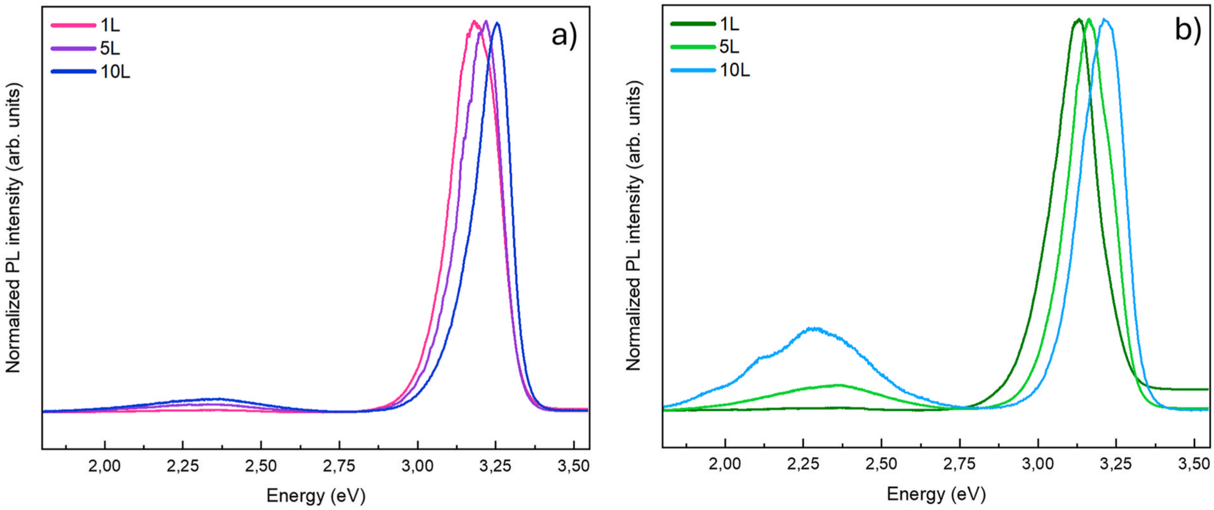

Fig. 8. μ-PL spectra of the same morphologies belonging to samples with different composition: long elongated structures in a) and clusters of elongated structures in b).

zinc (also in coordination VI) is 0.74 Å, this difference can cause mechanical stresses at the highest dopant content and lead to morphologies in which the symmetry of the crystal structure is not so well preserved, or in which different planar defects appear giving rise to changes in the growth directions as observed in some of the ribbons (Fig. 1 d). A particular kind of structure encountered in this sample is shown in Fig. 1 e. They consist of hexagonal rods that change the diameter at a certain growth step. The lower part of the rods has similar diameters to those described above, but the length of these rods is considerably reduced respect to those found in samples with lower Ru content. Hexagonal columns ending in a pyramid are very typical from ZnO. Grym et al. [28] reported the growth sequence of these kinds of structures. In our case, once the pyramid is formed, the growth does not completely stop, most likely due to an autocatalytic process giving rise to the upper narrower column.

As mentioned, the flux of the transport gas used during the treatment plays a determinant role on the morphology of the structures. Although some morphologies remain, as the large ribbons and wires shown in Fig. 2d and e the increase in the gas flux, causes radical changes and, new structures such as skewers, swords, and combs appear (Fig. 2). Insets of Fig. 2a and b clearly show the morphology of a triple-comb and a sword respectively. A typical skewer will be later studied in depth. These new structures are very long, reaching lengths of hundreds of micrometers. However, the dispersion in the widths is much lower. In the case of the swords, the width is quite homogeneous, around 14 μm, while in the skewers are in the range 2–4 μm and in the largest structures, the combs, reaches 20–30 μm. Hexagonal columns with irregular lateral faces, rods, ribbons and grids are also present. The height of hexagonal columns and the lengths of the rods are tens of micrometers, while their diameter varies between 850 nm and 6 μm. In this sense, combs are one of the characteristic structures observed in samples with the lowest Ru (Fig. 2 a). This is consistent with the fact that comb-like structures have been also obtained in undoped or very slightly cerium doped ZnO [29, 30]. In sample 1H, elongated structures predominate (Fig. 2 b). When the Ru content increases, sample 5H (Fig. 2 c), secondary growth is observed, however the branches are typically shorter than those obtained at low flux. Finally, in sample 10H, structures with changes in the growth direction are present as we have already observed in the sample 10L (Fig. 2 d). In this case ribbons are longer, and none or scarce grids and branched structures are found (Fig. 2 e).

Although the growth mechanism is very complex and no agreement has been yet attained, depending on the growth procedure, diffusion,

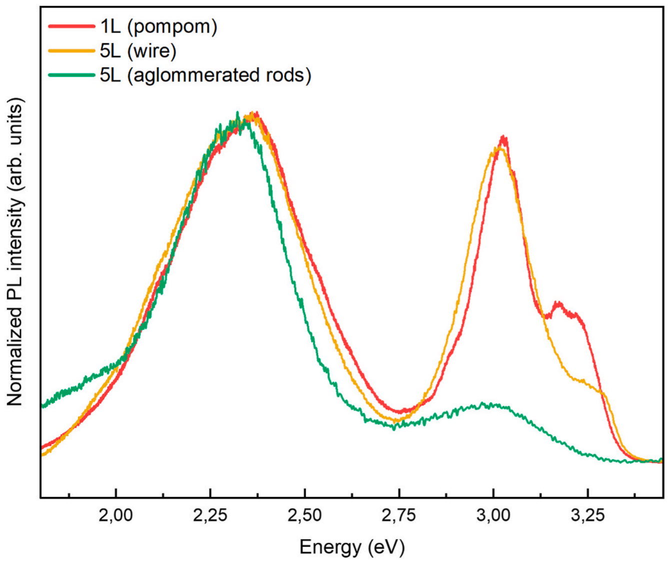

Fig. 9. μ-PL spectra of structures with violet emission growth onto the pellet. (For interpretation of the references to color in this figure legend, the reader is referred to the Web version of this article.)

Ostwald ripening or uneven dopant distribution, among others, have been claimed to have a role [31,32]. In the case of ZnO, with a wurtzite structure, the most energetic faces are the basal ones $\{0001\}$ type, the need to minimize the area of the high energy faces leads to a marked preferential growth along the c axis. However, the presence of defect or dopants might decrease this energy (due to non-saturated bonds, strains associated with different ionic radii or charge defect) promoted the growth along secondary directions. $[2\bar{1}\bar{1}0]$ or $[0\bar{1}10]$ rank second as fast-grow directions, that lead to ribbon-like structures. However, the incorporation of dopants gives rise to modifications in the surface energies, then changing the preferential growth directions and giving rise to different morphologies. These modifications have also been observed in previous works on doped ZnO structures grown by the same method [33,34]. Concretely, earlier investigations report that ruthenium modifies the preferential growth directions in ZnO [35,36] as well as causes some disorder in the growth of the structures [25]. In our case, the variety of morphologies obtained confirms the change in the growth directions. In Ref. [35], X-ray diffraction measurements reveal that growth along the c-axis is limited with an increase in Ru content, while reference [36] proposes a decrease in the stability of plane family surfaces $\{11\bar{2}0\}$. In our case, both hypotheses align with the observed morphologies, with Fig. 1b and c serving as good examples. The proposed crystallographic arrangement of these structures is shown in Fig. 3. The grid seems to be formed by a principal ribbon growth along the $[11\bar{2}0]$ direction and secondary ribbons following the directions of the same family, i.e., $[2\bar{1}\bar{1}0]$, $[\bar{1}2\bar{1}0]$, $[\bar{2}110]$, $[\bar{1}\bar{1}20]$ and $[1\bar{2}10]$. The sixfold star-like structure is probably composed of needle growth towards the c-axis, and secondary needles grow towards the directions of the $\langle 11\bar{2}0\rangle$ family.

To further investigate the crystallographic orientation of the grids and corroborate our growth model, EBDS measurements have been carried out. This characterization technique allows us to determine the face orientation of the structures through the diffraction pattern of back-scattered electrons. Fig. 4 shows the results of these experiments. Part a presents the color scale legend, which is used to identify crystallographic directions with colors in the EBSD orientation maps (part c). Parts b and c illustrate which crystallographic direction corresponds to each of the spatial axes (x, y, and z) of the sample. $[11\bar{2}0]$ is defined as the main growth direction, with the top and the bottom surfaces being $\{0001\}$ faces, and the secondary ribbons grow from $\{1\bar{1}00\}$ side surfaces towards the remaining $\langle 11\bar{2}0\rangle$ directions. This information is depicted on the secondary electron image of the grid in Fig. 4 d.

Representative μ-Raman spectra of the samples with each of the RuO_2 percentages are shown in Fig. 5 a. All the observed peaks correspond to active phonon modes for ZnO, more specifically to the wurtzite phase. Using the pure ZnO data as reference, 100 cm^{-1} and 439 cm^{-1} peaks are assigned to non-polar modes E_2^{low} and E_2^{high}, respectively. Peaks centered at 383 cm^{-1} and 410 cm^{-1} are attributed to the transversal optical phonon frequencies of the polar modes A1 and E1. Fig. 5 b draws a schematic representation of this vibration modes. In all the structures analyzed, the positions of the peaks are shifted to lower frequencies compared to pure ZnO. If, as extensively reported [22,36], ruthenium is incorporated into the ZnO lattice occupying substitutional Zn sites, this displacement would be attributed to the difference between Zn^{2+} mass (65.38 g/mol) and that of the Ru^{4+}(101.07 g/mol). The change in the effective mass may cause a reduction in the frequency of vibrational modes involving Zn ions. On the other hand, the stress induced by the ZnO lattice distortion may also contribute to the shift of the peaks. Due to the difference between ionic radii (Zn^{2+}: 0.74 Å, Ru^{4+}: 1.30 Å [22]), the replacement of Zn^{2+} ions by Ru^{4+} ions would increase the c lattice parameter, leading to changes on E_2^{high} frequency. Charge compensation must be considered as well. Since ruthenium cations are

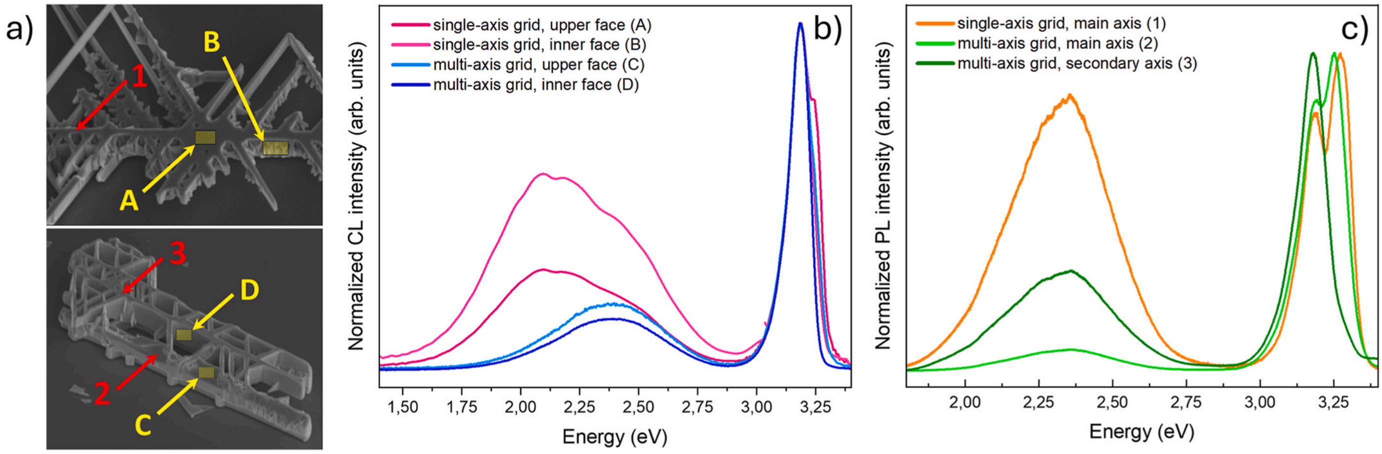

Fig. 10. a) SEM images of the two different types of grids: single-axis grid (top image) and multi-axis grid (bottom image). The areas where CL spectra were taken are delimited by light yellow rectangles, and yellow arrows. The red arrows point to the points where μ-PL spectra were measured. Normalized intensity CL (b) and μ-PL emission spectra (c) of different parts of grids present in sample 5H. In μ-PL spectra the aspect ratio between NBE and DB have been modified in order to obtain better resolution of defect band using a D2 filter. (For interpretation of the references to color in this figure legend, the reader is referred to the Web version of this article.)

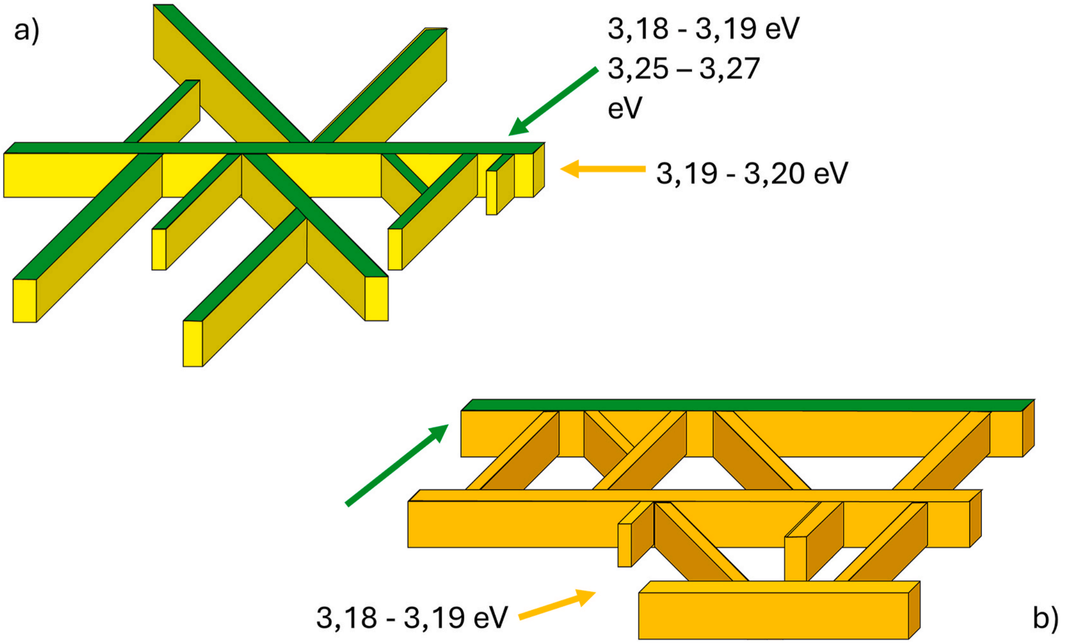

Fig. 11. Schematic structure of single-axis grid (a) and multi-axis grid (b), indicating the energy of its band-edge emission peaks.

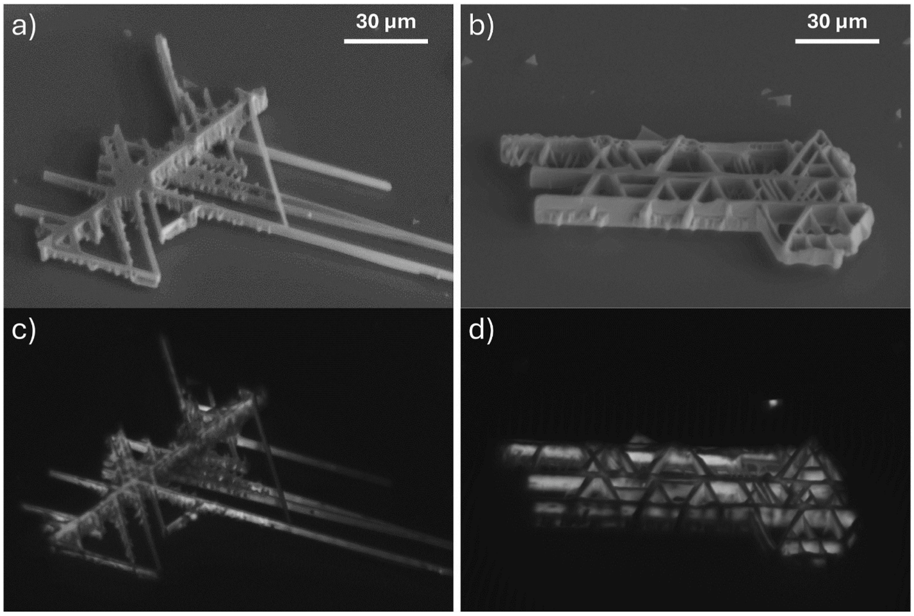

Fig. 12. SE images (a and b) and their corresponding panchromatic CL images (c and d) of grids present in sample 5H.

higher valence than zinc cations, the excess of positive charge could be compensated altering the density of some defects, for example creating zinc vacancies or decreasing oxygen vacancies.

In addition, a decrease in the intensity of the peaks as ruthenium content in the precursor powders increases is observed. This could be due to the deleterious effect of Ru doping. As have mentioned, the difference between ionic radii of Ru and Zn could be the cause of additional stresses, that would negatively affect the crystal quality. Particularly, E_2^{high}/E_2^{low} ratio decreases compared to ZnO but, within the group of doped samples, this ratio gently raises with the RuO_2 content (0.809 for 1 %, 0.851 for 5 % and 0.863 for 10 %). The E_2^{low} mode is mainly related to Zn vibrations, while E_2^{high} corresponds to O vibrations. Hence, the increase in E_2^{high}/E_2^{low} ratio may reflect the occupation of oxygen vacancies intrinsically present in zinc oxide [37]. This is consistent with the fact that we are not doping with metallic Ru but with ruthenium oxide, hence the more ruthenium oxide we incorporate into the precursor powders, the more oxygen there will be available during the synthesis of the material and the lower content of oxygen vacancies is expected.

The incorporation of Ru ions into the different structures was investigated by X-Ray microanalysis spectra and images (EDX). As expected, the samples with lower ruthenium oxide content in the precursors, exhibit a low Ru signal. In the case of low flux, grids from 1L content more ruthenium than any other kind of structure. However, when nitrogen flux increases, no Ru signal is detected. Although a much deeper study should be required to assess this point, changes in the composition of the supersaturated atmosphere above the substrate, could be behind this observation. It is worth to mention that for samples

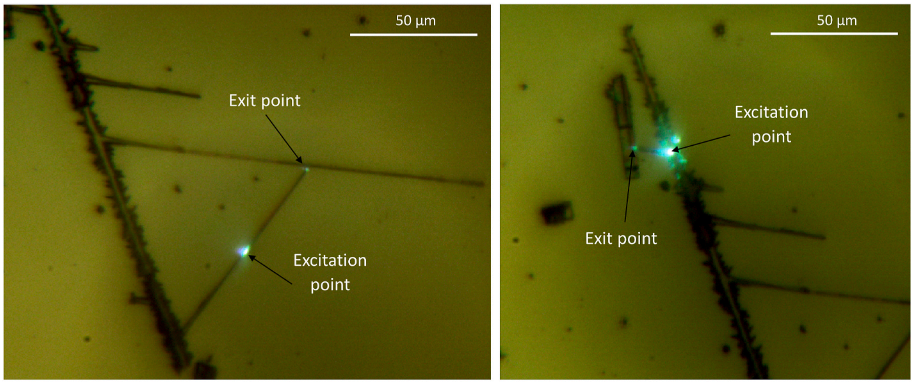

Fig. 13. Optical image of a grid with only some of its secondary growths developed.

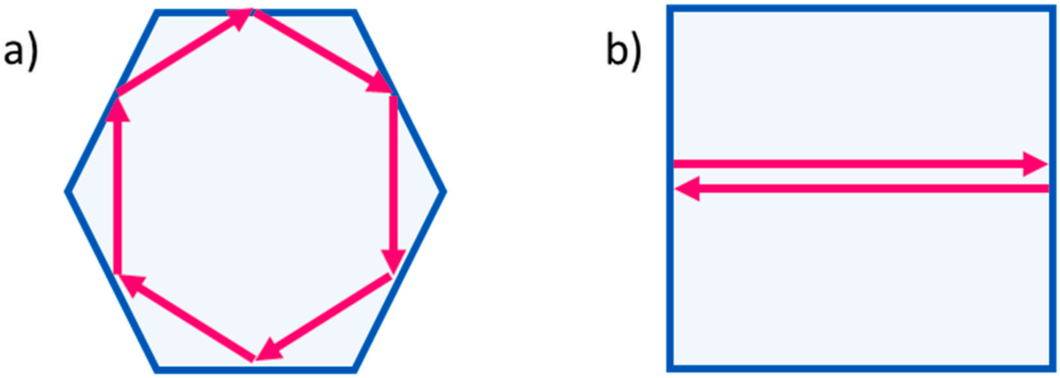

Fig. 14. Schematic representation of the optical paths (pink arrows) in a) a whispering gallery formed within a hexagonal structure and b) a Fabry – Pérot resonator. (For interpretation of the references to color in this figure legend, the reader is referred to the Web version of this article.)

with 1 wt % of RuO_2 in the precursor powders, the atomic percentage of Ru only represents 0.31 at. %, which is below the detection limit of the technique. Regarding 5 wt % RuO_2 samples, both 5L and 5H show similar results. Even though according to EDX measurements the ruthenium content is very low respect to the nominal values, the highest degree of incorporation was detected at the end of secondary growths and is greater than in 1L. This supports the idea that ruthenium affects the growth conditions, either acting as catalyst to secondary growths or promoting the growth along certain directions [38]. Reinforcing this hypothesis, in the 10 % wt. RuO_2 samples some big structures with several secondary growths that accumulate a large amount of dopant have been found. An example of this is presented in Fig. 6. In the SE image (part a of Fig. 6), it is observed that the structure has a high density of secondary growths at early growth stages. EDX maps (Fig. 6b and c and d) reveal a higher amount of ruthenium, and less oxygen and zinc in the structure than in the background structures. EDX spectra recorded in the area indicated in the figure reveal that in this type of incipient growths the amount of ruthenium can be as high as 29 % wt. Based on these observations, we suggest that the dopant is acting as catalyst for these type of ramifications [34]. Although the precursor for ZnO is ZnS, no traces of sulfur were detected, indicating that this element was properly eliminated during thermal treatment.

In order to complete the microstructural characterization, X-ray diffraction spectroscopy analysis was performed (Fig. 7). XRD patterns show peaks associable with ZnO wurtzite phase (JCPDS No. 00-036-1451) and hexagonal ruthenium (JCPDS No. 00-006-0663). The intensity of Ru related peaks increases as more RuO_2 is included in the precursor powders. Focusing on crusts (Fig. 7a), as expected for wurtzite structure, the most intense diffractions come from $(10\bar{1}0)$, (0002) and $(10\bar{1}1)$ Bragg planes. XRD patterns of the structures deposited on silicon are portrayed in Fig. 7b. There are no peaks corresponding to ruthenium or ruthenium oxide, indicating a good incorporation of Ru into the ZnO lattices. As the initial amount of ruthenium is increased, the intensity of all peaks is reduced, which is indicative of the loss of crystalline quality. Nevertheless, the most intense diffraction peak is not the (0002) as expected for ZnO, but the $(10\bar{1}3)$. A similar texturing was observed by Y. Ortega et al. in their microboxes [27]. They suggested that a high degree of Al incorporation (10 at. %) retards a directional growth, changing the preferential orientation. Thus, it is reasonable to think that the incorporation of Ru substituting Zn into ZnO lattice alters the dominant orientation, impeding the development of the structures along the typical growth directions.

Luminescence spectra at room temperature are taken from structures with the most characteristic morphologies of each sample. Both photoluminescence (PL) and cathodoluminescence (CL) spectra, and panchromatic CL images have been recorded. Combining both techniques, PL and CL, we will have an overall perspective of the electronic structure of the samples.

In all the collected spectra two main bands are observed: an ultraviolet band centered at 3.2 eV which corresponds to the near band edge emission, and a visible green band at 2.3 eV associated to the existence of defects in the ZnO structure. In general, structures obtained on the pellet show a stronger defect emission than those grown on the alumina boat, this effect was previously reported for this synthesis method [39].

In the case of the PL spectra of low flux samples (1L, 5L, and 10L), a blue shift of the UV peak is observed as Ru content increases. This shift of the band-edge is accompanied by a slight increment in the relative intensity of the green band. Despite this minor modification, variations in Ru content barely cause changes in the shape of the spectra. Fig. 8 shows the spectra of long elongated structures (part a) and clusters of elongated structures (part b) grown on the alumina boat. In both graphs it is possible to appreciate how the position of the band edge shifts from 3.18

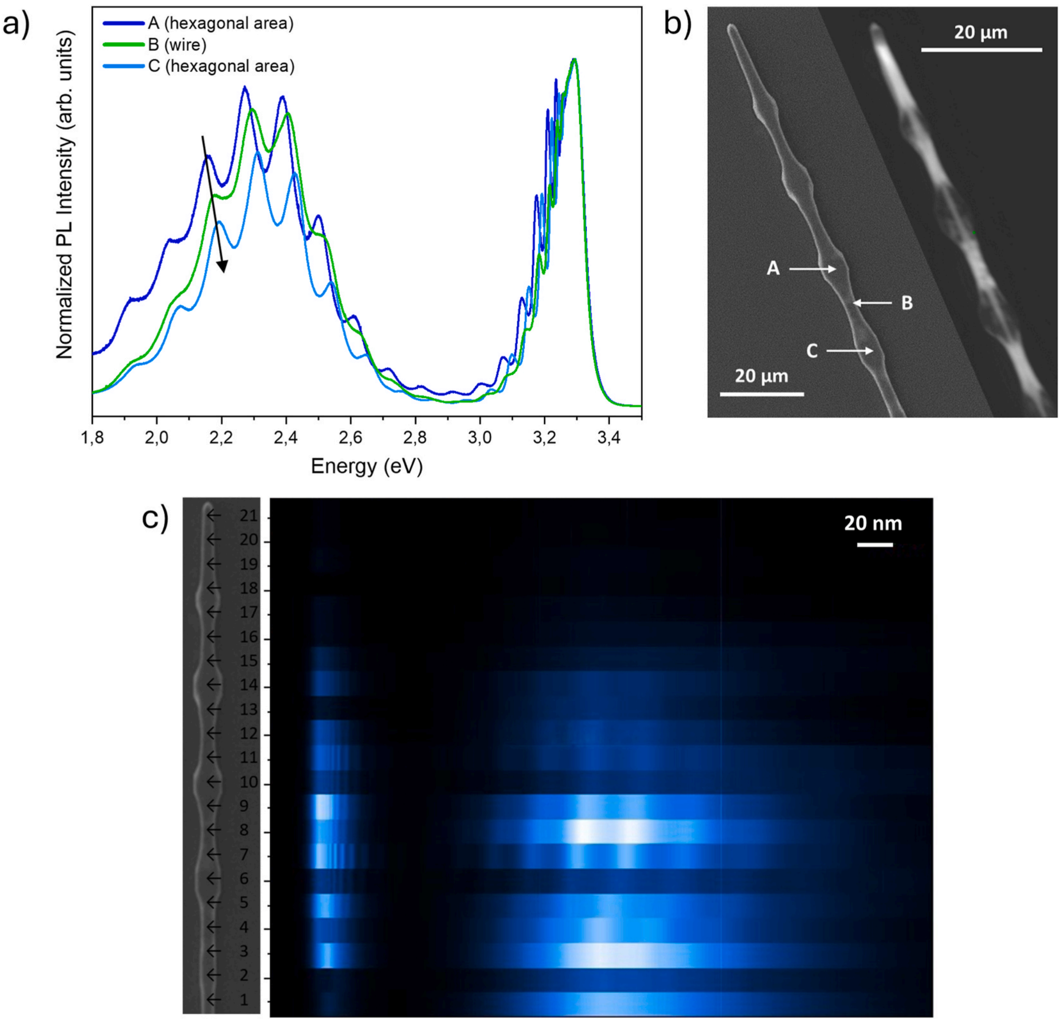

Fig. 15. a) Normalized intensity µ-PL spectra measured along a skewer in sample 1H, A and C spectra taken on the principal wire, and B and C taken on quasi-hexagonal protrusions. All of them show superimposed modulations not only in the visible range but also in the UV region. The narrow indicates how the resonant maxima change when the measuring point is distanced from the end of the structure. b) Secondary electron image and CL-panchromatic image of the skewer, the measured points are marked. c) Map of the evolution of the µ-PL emission along the structure.

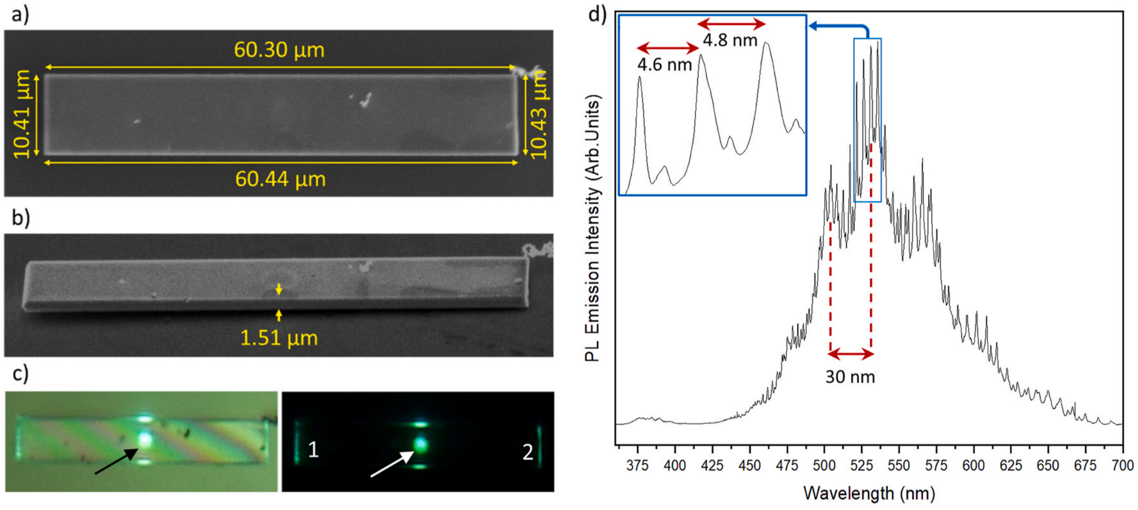

Fig. 16. a), b) SEM images showing the dimensions of studied ribbon. c) µ-PL images of the ribbon, under illumination (left) and in dark (right). The excitation point is marked with an arrow. d) Spectrum recorded at excitation point, where two main sets of peaks relatives to resonant cavities are clearly appreciable. Red arrows represent the wavelength difference between modulation peaks. (For interpretation of the references to color in this figure legend, the reader is referred to the Web version of this article.)

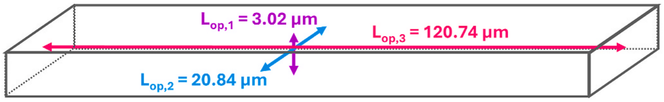

Fig. 17. Schematic representation of ribbon, including optical path lengths calculated for FP cavity.

eV to 3.27 eV and 3.13 eV–3.21 eV respectively as the percentage of ruthenium increases. In addition, the increase in the relative intensity of the green visible band is also noticeable. Previous works report that the bandgap decreases [40,41] or remains unaltered [13] upon ruthenium incorporation, in our case the band gap energy increases with ruthenium content. This raise may indicate a Burstein-Moss (B-M) effect, already reported by F. Sarf et al. [42].

Looking at the structures nucleated onto the pellet in low flux samples, we found a characteristic type of spectra which exhibit a violet band centered at around 3.06 eV as well as a stronger green emission (Fig. 9). This violet emission has been previously observed and may imply that the incorporation of ruthenium leads to the appearance of zinc vacancies due to the charge unbalance. As ruthenium has a higher valence than zinc, its incorporation into ZnO lattice could lead to an excess of charge. To alleviate this effect, an ionic compensation takes place, whereby the excess of charge is balanced by creating crystal defects. In our case, assuming ruthenium in oxidation state (IV), it would be necessary one zinc vacancy to compensate each Ru ion [43]. The emission peaked at 3.06 eV is assigned to electronic decay from conduction band to V_{Zn} [44]. In some cases, the violet peak has a shoulder that appears at higher energy. It seems that the presence of the mentioned shoulder in the UV region results in a blue shift of the defect emission band. We thought that this shoulder is ascribed to the near band edge emission, as it suffers a similar shift with Ru to the B-M effect already discussed. Defect bands are centered in 2.32 eV and 2.36 eV. The fact that the defect emission band is predominant over the near band edge suggests that the incorporation of ruthenium also increases the defects density.

As mentioned above the presence of ruthenium in the precursor powders produces grids in both low and high flux samples. When the grid is in the early stages of its development, the spectra of the central axis and that of the secondary growths are very similar. A band edge located at 3.25–3.27 eV accompanied by an emission centered at 3.19–3.2 eV are observed in PL spectra in both cases. The higher energy component is barely appreciable in CL. The main difference between the luminescence from the two parts of the structure lies in a slight increase in the relative intensity of the defect band in the case of secondary growths. When secondary growths develop, there are two paths in the evolution of the structure, leading to two different types of grids: single-axis grids and multi-axis grids (see Fig. 10 a). Single-axis grids are composed of a long main axis from which ribbons grow forming angles of 60° and 120°. By contrast, in the multi-axis grids, we found ribbons parallels to the main axis breaking the development of tilted ribbons. We can see the two resulting grid types in the SEM images in the part a of Fig. 10, the locations of luminescence spectra are also indicated: CL and PL spectra in parts b and c of the same figure. In single-axis grids, we see that the upper faces of the ribbons have the UV emission divided into two bands, located at 3.18–3.19 eV and at 3.24–3.27 eV, while in the rest of the structure only the band centered at 3.19–3.2 eV is observed. However, in multi-axis grids, all the faces give the same UV emission, centered at 3.18–3.19 eV, except the upper face of the outermost horizontal ribbon of the structure, the so-called main axis, where the emission is composed by two bands in 3.18–3.19 eV and 3.25 eV. This spatial distribution of the UV emission is illustrated in Fig. 11. It is also noticeable how the intensity of the different bands which compose the green emission changes, indicating that the defect structure changes between the different grids. For single-axis grid, the maximum of the band shifts to lower energies, evidencing a higher density of deeper defect states in this grid comparing with multi-axis-grid.

Fig. 12 shows secondary electron images (parts a and b) and panchromatic CL images (parts c and d) of the two types of grids already mentioned. From luminescence images, the single-axis grid reveals a brighter internal skeleton. Comparing CL images and spectra it is possible to know that the main luminesce intensity comes from the NBE emission. In the multi-axis grid the luminescence contrast is associated to differences between the flat part of the inner faces and those with secondary growths. The intensity of band edge emission is higher in the flat part, indicating better crystallization.

Finally, the behavior of the structures as waveguides and optical resonators has also been investigated by μ-PL experiments. High refractive index of ZnO (n ~ 2) in the visible spectral region makes possible the light confinement within the material, thus ZnO structures are excellent candidates as resonant cavities and light guides [6,8,40]. The waveguiding behavior in an elongated structure from sample 5L is shown in Fig. 13. The laser is focused on the excitation point marked on the μ-PL image. The excited luminescence is only observed at the end of

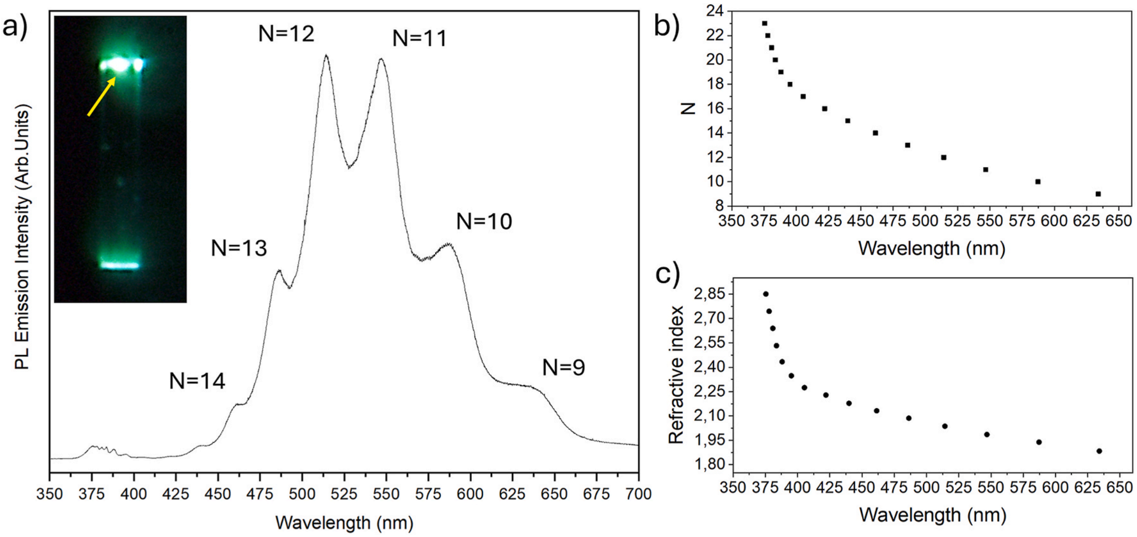

Fig. 18. a) μ-PL spectrum recorded at the end of the ribbon, where only a set of modulations take place. The inset corresponds to image of the ribbon in dark. The excitation point is marked with an arrow. b) Order of interference obtained from the wavelength position of the resonant peaks. Some of them are indicated in the spectrum. c) Calculated value of refractive index.

the secondary growth (exit point), with no losses along the structure length indicating efficient light guiding along it.

In addition, resonances are observed in the luminescence spectra of the structures analyzed appearing as a series of maxima superimposed to the typical luminescence bands already discussed.

Modulations can be attributed to whispering gallery (WG) or Fabry-Pérot (FP) modes depending on the geometry of the structure and the optical path followed by light, both are illustrated in Fig. 14. In the case of whispering galleries, the light is guided within the structure by successive internal reflections forming a closed optical path. In the case of an interface air/ZnO (n = 2.02 at $\lambda = 550$ nm), the critical angle obtained by the Snell law is 29.67° (Fig. 14 a). In the case of Fabry-Pérot resonators consist of two parallel mirrors (Fig. 14 b).

The variety of morphologies exhibited by the ZnO:Ru samples makes particularly interesting the study of their behavior as optical cavities. Among the morphologies observed, swords, skewers, and grids (single-axis and multi-axis grids) present modulations are especially interesting. Due to the complex geometry that some of the structures possess, we will discuss in a general way the observations in a skewer from 1H, and we will analyze in detail the optical resonances on a short ribbon from 10H.

Skewers typically show optical resonant modes not only at hexagonal shaped areas but also at the central wire. Fig. 15 a shows several spectra taken at the points marked on the SEM image of a skewer (part b of Fig. 15). An important feature is that the spectra are modulated over the entire energy range, that is, this kind of structures can act as resonant cavities for wavelengths in the whole visible range and also in part of the ultraviolet range. Looking at the PL spectra, it is possible to see how the maxima of the resonant peaks shift to higher energies as the collecting point moves towards the edge of the structure, which means that the optical path smoothly decreases in this direction. In order to assess the behavior of the different parts of the structure, the PL emission map was obtained (part c of Fig. 15). Far from the end, luminescence is almost suppressed in the quasi-hexagonal protrusions. The UV emission is more intense at the junctions of these protrusions and the main wire. Finally, at the end of the skewer the signal is almost vanished probably due to poorer crystallinity.

Fig. 16 shows the SEM images of a ribbon grown on the sample with 10 wt % Ru on the alumina boat (parts a and b), the μ-PL images of the same ribbon (part c) and its corresponding μ-PL spectrum (part d). Firstly, it is possible to observe its behavior as waveguide: the luminescence generated by the laser incidence, at the point marked by the arrow, is guided along the horizontal axes of the structure and exits at the end of the longitudinal axis (points 1 and 2). In addition to waveguiding phenomenon, two different superimposed modulations are clearly visible in the spectrum, showing how this ribbon also works as a double resonant cavity. Regarding to previously explained resonant cavities and the fact that to support a total internal reflection is mandatory in whispering gallery modes, the dimensions of the investigated ribbon allow us to exclude the possibility of whispering gallery formation, indicating that both sets of modulations correspond to two different FP cavities.

In this case, light will constructively interfere for those wavelengths that satisfy the following condition:

$$\lambda = n(\lambda) \bullet L_{op} / N \tag{1}$$

Where n is the refractive index, L_{op} is the optical path and N is the order of interference. Accordingly, the separation between maxima is given by:

$$\Delta\lambda = \frac{\lambda^2}{L_{op} \bullet \left(n - \lambda \frac{dn}{d\lambda}\right)} \tag{2}$$

Considering the optical path lengths showed at Fig. 17, and using an approximation of eq (2) such that $\Delta\lambda = \lambda^2/n \cdot L_{op}$, the corresponding $\Delta\lambda$ are $\Delta\lambda_1 = 44.87$ nm, $\Delta\lambda_2 = 6.50$ nm and $\Delta\lambda_3 = 1.12$ nm at $\lambda = 525$ nm (n = 2.034). The last wavelength difference results too small for the resolution of our detection system, while $\Delta\lambda_1 = 44.87$ nm and $\Delta\lambda_2 = 6.50$ nm are in good agreement with peaks observed at Fig. 16d.

In order to analyze the resonances that take place on the vertical axis, a carefully chosen spectrum was taken in which only these modulation peaks are present. The result are shown in Fig. 18.

At the position of the measurement, the FP optical path is 3.02 μm as measured in the SEM image. Making use of eq (1), and taking from Ref. [6] the expression of wavelength-dependant refractive index for bulk ZnO, we can obtain the order of interference N (Fig. 18 a). Then, an approximate value of the refractive index of our material is estimated knowing L_{op}, N and λ. The estimated value of n as well as N are showed in Fig. 18b and c.

4. Conclusions

In this study, we have proved the significant influence of Ru content on the morphology of doped ZnO, including changes in shape, size, density of secondary growths, and preferential orientation. EDX measurements have also confirmed the proper incorporation of dopant ions. The crystal quality of the samples has been assessed by XRD and Raman experiments. Besides the wurtzite structure, typical of ZnO, a residual Ru phase has been also detected. The shifts seen in the Raman peaks indicate that Ru4+ occupies Zn2+ sites, leading to consequent lattice distortion. As expected, the addition of Ru has also had a major influence on the electronic structure of ZnO. Broadening of the bandgap with increasing Ru content attributed to the Moss-Burstein effect has been observed in μ-PL spectra. Some structures showed an intense emission around 3.06 eV, likely due to zinc vacancies generated as compensation mechanism due to the charge difference between Ru (+4) and Zn (+2) ions. We have extensively studied the luminescence of grids as a characteristic morphology of Ru-doped ZnO, assessing UV emission and changes in the defect structure. Furthermore, the properties of our samples as waveguides and Fabry-Pérot resonant cavities have been thoroughly studied.

CRediT authorship contribution statement

Rodríguez-Peña Micaela: Writing – review & editing, Writing – original draft, Visualization, Validation, Methodology, Investigation, Formal analysis. **Sotillo Belén:** Writing – review & editing, Validation, Investigation. **Urbieta Ana:** Writing – review & editing, Writing – original draft, Validation, Supervision, Methodology, Investigation, Conceptualization. **Fernández Paloma:** Writing – review & editing, Validation, Supervision, Resources, Project administration, Methodology, Funding acquisition, Conceptualization.

Declaration of competing interest

The authors declare that they have no known competing financial interests or personal relationships that could have appeared to influence the work reported in this paper.

Acknowledgments

This work has been financed by Comunidad de Madrid under Project PR65/19–22464 (Proyectos de I + D para jóvenes doctores) and Universidad Complutense de Madrid under project PR3/23–30813.

References

[1] S.J. Pearton, F. Ren, Advances in ZnO-Based Materials for Light Emitting Diodes, Elsevier Ltd., 2014, https://doi.org/10.1016/j.coche.2013.11.002.

[2] F. Rahman, Zinc oxide light-emitting diodes: a review, Opt. Eng. 58 (1) (Jan. 2019) 1, https://doi.org/10.1117/1.oe.58.1.010901.

[3] L. Shi, H. Shen, L. Jiang, X. Li, Co-emission of UV, violet and green photoluminescence of ZnO/TiO2 thin film, Mater. Lett. 61 (25) (Oct. 2007) 4735–4737, https://doi.org/10.1016/j.matlet.2007.03.019.

[4] S. Rühle, L.K. Van Vugt, H.Y. Li, N.A. Keizer, L. Kuipers, D. Vanmaekelbergh, Nature of sub-band gap luminescent eigenmodes in a ZnO nanowire, Nano Lett. 8 (1) (Jan. 2008) 119–123, https://doi.org/10.1021/nl0721867.

[5] R. Chen, B. Ling, X.W. Sun, H.D. Sun, Room temperature excitonic whispering gallery mode lasing from high-quality hexagonal ZnO microdisks, Adv. Mater. 23 (19) (May 2011) 2199–2204, https://doi.org/10.1002/adma.201100423.

[6] R. Ariza, B. Sotillo, F. Pavón, A. Urbieta, P. Fernández, Evolution of whispering gallery modes in Li-doped ZnO hexagonal micro-and nanostructures, Appl. Sci. 10 (23) (Dec. 2020) 1–13, https://doi.org/10.3390/app10238602.

[7] P. Singh, R. Kumar, R.K. Singh, Progress on transition metal-doped ZnO nanoparticles and its application, Am. Chem. Soc. (Sep. 18, 2019), https://doi.org/10.1021/acs.iecr.9b01561.

[8] F. Pavón, A. Urbieta, P. Fernández, Luminescence and light guiding properties of Er and Li codoped ZnO nanostructures, J. Lumin. 195 (Mar. 2018) 396–401, https://doi.org/10.1016/j.jlumin.2017.11.059.

[9] A. Urbieta, R. Del Campo, R. Pérez, P. Fernández, J. Piqueras, Luminescence and waveguiding behavior in Tb doped ZnO micro and nanostructures, J. Alloys Compd. 610 (Oct. 2014) 416–421, https://doi.org/10.1016/j.jallcom.2014.05.007.

[10] F. Pavón, A. Urbieta, P. Fernández, Characterization, luminescence and optical resonant modes of Eu-Li Co-doped ZnO nano- and microstructures, Appl. Sci. 12 (14) (Jul. 2022), https://doi.org/10.3390/app12146948.

[11] R. Ariza, A. Urbieta, J. Solis, P. Fernández, Optical properties of 2D micro- and nanostructures of ZnO:K, Materials 15 (21) (Nov. 2022), https://doi.org/10.3390/ma15217733.

[12] K. Habanjar, D. Dasuki, R. Awad, M. Rekaby, Optical and magnetic behaviors of Ru-doped ZnO nanoparticles, J. Supercond. Nov. Magnetism (2022), https://doi.org/10.1007/s10948-022-06302-9.

[13] J.Z. Bloh, R. Dillert, D.W. Bahnemann, Transition metal-modified zinc oxides for UV and visible light photocatalysis, Environ. Sci. Pollut. Control Ser. 19 (9) (Nov. 2012) 3688–3695, https://doi.org/10.1007/s11356-012-0932-y.

[14] S. Khan, S.S. Shah, A.B. Yurtcan, A.A.A. Bahajjaj, A. Zafar, N.K. Janjua, Electrooxidation of ammonia at high-efficiency RuO2-ZnO/Al2O3 and PdO-ZnO/Al2O3 mesoporous catalysts; an innovative strategy towards clean fuel technology, Fuel 347 (Sep) (2023), https://doi.org/10.1016/j.fuel.2023.128446.

[15] S. Khan, et al., Ruthenium and palladium oxide promoted zinc oxide nanoparticles: efficient electrocatalysts for hydrazine oxidation reaction, J. Electroanal. Chem. 917 (Jul) (2022), https://doi.org/10.1016/j.jelechem.2022.116422.

[16] D. Amaranatha Reddy, R. Ma, T.K. Kim, Efficient photocatalytic degradation of methylene blue by heterostructured ZnO-RGO/RuO2 nanocomposite under the simulated sunlight irradiation, Ceram. Int. 41 (5) (Jun. 2015) 6999–7009, https://doi.org/10.1016/j.ceramint.2015.01.155.

[17] S. Khan, et al., Ruthenium and palladium oxide promoted zinc oxide nanoparticles: efficient electrocatalysts for hydrazine oxidation reaction, J. Electroanal. Chem. 917 (Jul) (2022), https://doi.org/10.1016/j.jelechem.2022.116422.

[18] C.S. Vennapoosa, et al., Single-atom Ru catalyst-decorated CNF(ZnO) nanocages for efficient H2 evolution and CH3OH production, J. Phys. Chem. Lett. 14 (50) (Dec. 2023) 11400–11411, https://doi.org/10.1021/acs.jpclett.3c02347.

[19] Ş. Karataş, H.M. El-Nasser, A.A. Al-Ghamdi, F. Yakuphanoglu, High photoresponsivity Ru-doped ZnO/p-Si heterojunction diodes by the sol-gel method, Silicon 10 (2) (Mar. 2018) 651–658, https://doi.org/10.1007/s12633-016-9508-7.

[20] K.R. Aranganayagam, S. Senthilkumaar, N. Ganapathi Subramaniam, Studies on structural, optical and magnetic properties of (Ru, Mn) codoped ZnO nanostructures, in: IOP Conference Series: Materials Science and Engineering, Institute of Physics Publishing, Mar. 2018, https://doi.org/10.1088/1757-899X/310/1/012009.

[21] Q. Wang, Y. Gu, C. Chen, F. Pan, C. Song, Oxide spintronics as a knot of physics and chemistry: recent progress and opportunities, Am. Chem. Soc. (Nov. 03, 2022), https://doi.org/10.1021/acs.jpclett.2c02634.

[22] S. Kumar, et al., Structural, optical and magnetic characterization of Ru doped ZnO nanorods, J. Alloys Compd. 588 (Mar. 2014) 705–709, https://doi.org/10.1016/j.jallcom.2013.11.137.

[23] D. Dasuki, K. Habanjar, R. Awad, Effect of growth and calcination temperatures on the optical properties of ruthenium-doped ZnO nanoparticles, Condens Matter 8 (4) (Dec. 2023), https://doi.org/10.3390/condmat8040102.

[24] S.Y. Yun, G.B. Cha, Y. Kwon, S. Cho, S.C. Hong, First-principles calculations on magnetism of transition metal doped zinc oxide, in: Journal of Magnetism and Magnetic Materials, Elsevier, 2004, https://doi.org/10.1016/j.jmmm.2003.12.566.

[25] Y. Shao, et al., Electronic structure and enhanced photoelectrocatalytic performance of RuxZn1−xO/Ti electrodes, Journal of Advanced Ceramics 10 (5) (Oct. 2021) 1025–1041, https://doi.org/10.1007/s40145-021-0486-x.

[26] L. Khomenkova, P. Fernández, J. Piqueras, ZnO nanostructured microspheres and elongated structures grown by thermal treatment of ZnS powder, Cryst. Growth Des. 7 (4) (Apr. 2007) 836–839, https://doi.org/10.1021/cg060789a.

[27] Y. Ortega, P. Fernández, J. Piqueras, Al doped ZnO nanoplate arrays and microbox structures grown by thermal deposition, J. Appl. Phys. 105 (5) (2009), https://doi.org/10.1063/1.3079523.

[28] J. Grym, P. Fernández, J. Piqueras, Growth and spatially resolved luminescence of low dimensional structures in sintered ZnO, Nanotechnology 16 (6) (Jun. 2005) 931–935, https://doi.org/10.1088/0957-4484/16/6/051.

[29] M. Rodríguez-Peña, G. Flores-Carrasco, A. Urbieta, M.E. Rabanal, P. Fernández, Growth and characterisation of ZnO micro/nanostructures doped with cerium for photocatalytic degradation applications, J. Alloys Compd. 820 (Apr) (2020), https://doi.org/10.1016/j.jallcom.2019.153146.

[30] T. Xu, P. Ji, M. He, J. Li, Growth and structure of pure ZnO micro/nanocombs, J. Nanomater. 2012 (2012), https://doi.org/10.1155/2012/797935.

[31] F. Lorenzo, et al., Direct imaging of dopant distribution in polycrystalline ZnO films, ACS Appl. Mater. Interfaces 9 (8) (Mar. 2017) 7241–7248, https://doi.org/10.1021/acsami.6b14350.

[32] S. Allami, ZnO nanowire hydrothermal synthesization: parameters affecting their growth direction and surface morphology parameters affecting their growth direction and surface morphology. www.intechopen.com, 2016.

[33] F. Pavón, A. Urbieta, P. Fernández, Luminescence and light guiding properties of Er and Li codoped ZnO nanostructures, J. Lumin. 195 (Mar. 2018) 396–401, https://doi.org/10.1016/j.jlumin.2017.11.059.

[34] A. Urbieta, P. Fernández, J. Piqueras, Nanowires and stacks of nanoplates of Mn doped ZnO synthesized by thermal evaporation-deposition, Mater. Chem. Phys. 132 (2–3) (Feb. 2012) 1119–1124, https://doi.org/10.1016/j.matchemphys.2011.12.084.

[35] R. Vettumperumal, S. Kalyanaraman, R. Thangavel, Effect of ruthenium concentration on structural and I-V characteristics of ZnO thin films by sol–gel method, J Mol Eng Mater 5 (1) (Mar. 2017) 1750004, https://doi.org/10.1142/s2251237317500046.

[36] I. Iwantono, S.K. Md Saad, R. Yuda, M.Y. Abd Rahman, A.A. Umar, Structural and properties transformation in ZnO hexagonal nanorod by ruthenium doping and its effect on DSSCs power conversion efficiency, Superlattice. Microst. 123 (Nov. 2018) 119–128, https://doi.org/10.1016/j.spmi.2018.05.041.

[37] Hiroaki Fukushima, Hiroshi Uchida, Hiroshi Funakubo, Takashi Katoda, Ken Nishida, Evaluation of Oxygen Vacancies in ZnO Single Crystals Andpowders by Micro-raman Spectroscopy, Ceramic Society of Japan, Jun. 01, 2017, https://doi.org/10.2109/jcersj2.16262.

[38] I. Iwantono, S.K. Md Saad, R. Yuda, M.Y. Abd Rahman, A.A. Umar, Structural and properties transformation in ZnO hexagonal nanorod by ruthenium doping and its effect on DSSCs power conversion efficiency, Superlattice. Microst. 123 (Nov. 2018) 119–128, https://doi.org/10.1016/j.spmi.2018.05.041.

[39] R.A. García, Micro-y nanoestructuras de ZnO dopado con metales: síntesis y crecimiento ordenado sobre sustratos estructurados por láser. Departamento de Física de Materiales, Univ. Complutense, Madrid, España, 2022. PhD dissertation.

[40] P.K. Singh, N. Singh, M. Singh, S.K. Singh, P. Tandon, Development and characterization of varying percentages of Ru-doped ZnO (xRu:ZnO; $1\% \leq x \leq 5\%$) as a potential material for LPG sensing at room temperature, Appl. Phys. Mater. Sci. Process 126 (5) (May 2020), https://doi.org/10.1007/s00339-020-3439-2.

[41] M.E. Manríquez, et al., One-pot synthesis of ru-doped ZnO oxides for photodegradation of 4-chlorophenol, Int. J. Photoenergy 2018 (2018), https://doi.org/10.1155/2018/7605306.

[42] F. Sarf, I. Karaduman Er, E. Yakar, S. Acar, The role of rare-earth metal (Y, Ru and Cs)-doped ZnO thin films in NH3 gas sensing performances at room temperature, J. Mater. Sci. Mater. Electron. 31 (13) (Jul. 2020) 10084–10095, https://doi.org/10.1007/s10854-020-03554-w.

[43] J.Z. Bloh, R. Dillert, D.W. Bahnemann, Ruthenium-modified zinc oxide, a highly active vis-photocatalyst: the nature and reactivity of photoactive centres, Phys. Chem. Chem. Phys. 16 (12) (Mar. 2014) 5833–5845, https://doi.org/10.1039/c3cp55136a.

[44] X.M. Fan, J.S. Lian, L. Zhao, Y.H. Liu, Single violet luminescence emitted from ZnO films obtained by oxidation of Zn film on quartz glass, Appl. Surf. Sci. 252 (2) (Oct. 2005) 420–424, https://doi.org/10.1016/j.apsusc.2005.01.018.